ELSEVIER

Applied Surface Science 162–163 (2000) 519–528

applied surface science

www.elsevier.nl/locate/apsusc

Physical properties of self-assembled nanosized cobalt particles

C. Petit [a,b], M.P. Pileni [a,b,*]

[a] *Université Pierre et Marie Curie, Laboratoire SRSI, URA CNRS 1662, 4 Place Jussieu, 75251 Paris Cedex, France*
[b] *CEA-Saclay, DSM-DRECAM-SCM, 91191 Gif sur Yvette Cedex, France*

Abstract

Fabrication, structural, magnetic and local electronic properties of cobalt metallic nanocrystals are reported. Nanosized cobalt particles are synthesized in colloidal assemblies. After surface passivation and extraction of the nanocrystals from the micellar media, cobalt nanoparticles with a narrow size distribution are obtained. The particles are then stable under air. Deposited on a surface, the nanoparticles form a 2D hexagonal network spontaneously.

The magnetic properties are strongly dependent on the self-organization of cobalt nanocrystals. In a 2D self-assemblies, collective properties originated from the dipolar magnetic interaction between adjacent particles are observed.

Isolated particles are studied by scanning tunneling microscopy at room temperature under air. The spectroscopy experiments performed at 77 K show well-resolved Coulomb gap and Coulomb staircase features.

Keywords: Magnetism; STM; Nanoparticles; Self-assembly; Cobalt

1. Introduction

The synthesis of nanosized particles, with a well-defined size and shape is an achievement that will have important consequences in many fields of nanotechnology [1]. This nanocrystals has been shown to form the basis for fabrication of lithographic masks [2], ultramicroelectrodes from gold nanoparticles [3] or been used to study new quantum phenomena leading to new electronic devices such as single electron tunneling transistors [4,5]. On the other hand, since the characteristic energy involved in single electron tunneling decreases rapidly with increase of the device size, the particles must be only of few nanometers in diameter [6–8] in order to surmount the problem of thermal fluctuations at room temperature. It is possible to reach this size limit using different physical (see for example, Ref. [9]) or chemical processes [10,11] to obtain nanosized particles.

However, for operating nanosized-particles-based devices at room temperature, it is necessary to fabricate conductive islands separated by well-defined tunneling barriers organized in a well-defined periodical structures. Recent progress in colloidal chemistry [10] has made this possible for some metals and semiconductors. 2D and 3D self-assembled structures of semiconductor [13,14] or metallic particles [6,15–19] have been obtained. We succeed also in forming self-assembled arrays of ferromagnetic nanoparticles [20,21]. Such self-assembly shows spe-

Abbreviations: 73.23 Hk; 75.70 Ak; 81.20. Ka; 82.70Dd

* Corresponding author. Université Pierre et Marie Curie, Laboratoire SRSI, URA CNRS 1662, 4 Place Jussieu, 75251 Paris Cedex, France. Tel.: +33-1-44-27-25-16; fax: +33-1-44-27-25-15.
E-mail address: pileni@sri.jussieu.fr (M.P. Pileni).

0169-4332/00/$ - see front matter
PII: S0169-4332(00)00243-9

cific properties to be quite different from those of isolated nanosized particles or bulk materials [12,20,21].

In this paper, structural and self-organization of cobalt nanocrystals are described by transmission electron microscopy (TEM), X-ray diffraction (XRD) and small-angle X-ray scattering (SAXS). Comparison of magnetic properties of similar nanocrystals either dispersed in a solvent (considered as isolated) or organized in 2D superlattices on graphite HOPG is presented. Finally, STM/STS data on the organization and local electronic properties of Co nanocrystals deposited on the dodecanthiol self-assembled monolayer (SAM) are presented.

2. Experimental section

2.1. Products

All materials were used without further purification. $CoCl_2$, AOT and sodium borohydride, $NaBH_4$, were purchased from Sigma, isooctane from Fluka. The synthesis of $Co(AOT)_2$ has been described else-

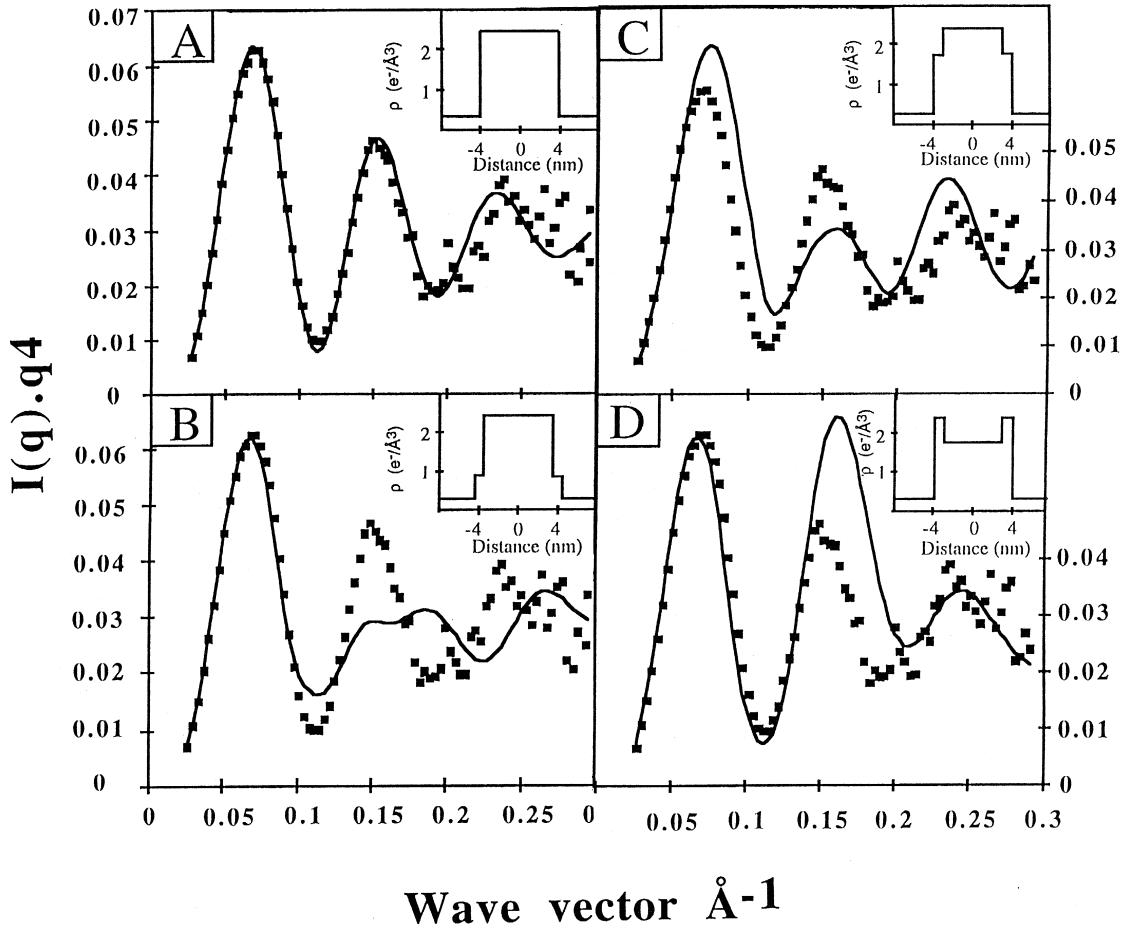

Fig. 1. SAXS data for cobalt nanosized particles after redispersion in pyridine. Porod's representation. The points represent the experimental data. The solid line is the best adjustment assuming a sphere with gaussian polydispersity. Insert is the electronic density profil used for the simulation. (A) Homogeneous particles of cobalt (8 nm). (B) Particles of cobalt (6 nm) surrounded by a shell of B_2O_3. (C) Particles of cobalt (6 nm) surrounded by a shell of cobalt boride. (D) Particles of cobalt borides (6 nm) surrounded by a shell of cobalt.

where [21]. $Co(AOT)_2$ is used as a stock solution at 0.125 M in isooctane.

2.2. Apparatus

TEM image and electron diffraction spectroscopy (EDS) patterns were obtained with a JEOL 100CX2 microscope. The solution was placed on a carbon-coated copper grid and evaporated under a nitrogen atmosphere. XRD measurements were carried out using a STOE Stadi P goniometer with a Siemens Kristalloflex X-ray generator with a cobalt anticathode ($\lambda = 1.7809$ Å) driven by a personal computer through a DACO-MP Interface. The magnetic studies were performed using a commercial SQUID magnetometer Cryogenic S600. The STM/STS experiments were performed at room temperature as well as at low temperature (77 K) using a home-built STM/STS [24]. 3D organization is observed with an Omicron STM VT apparatus operating at 77 K.

3. Result

3.1. Synthesis

In our previous papers [20,21], the synthesis of cobalt nanocrystals, using reverse micelles as a microreactor, has been described. Cobalt particles are obtained by mixing two micellar solutions having the same diameter (3 nm): one contains 10^{-2} M cobalt bis(2 ethyl-hexyl)-sulfosuccinate ($Co(AOT)_2$) and the other one 2×10^{-2} M of sodium tetrahydroboride ($NaBH_4$). After mixing, the micellar solution remains optically clear and its color turns immediately from pink to black, indicating the formation of colloidal particles. The particles are highly dispersed and no aggregation occurs. They are extracted from reverse micelles under anaerobic conditions, by covalent attachment of either tri-octyl-phosphine and redispersed in pyridine (particles **I**) or coated by

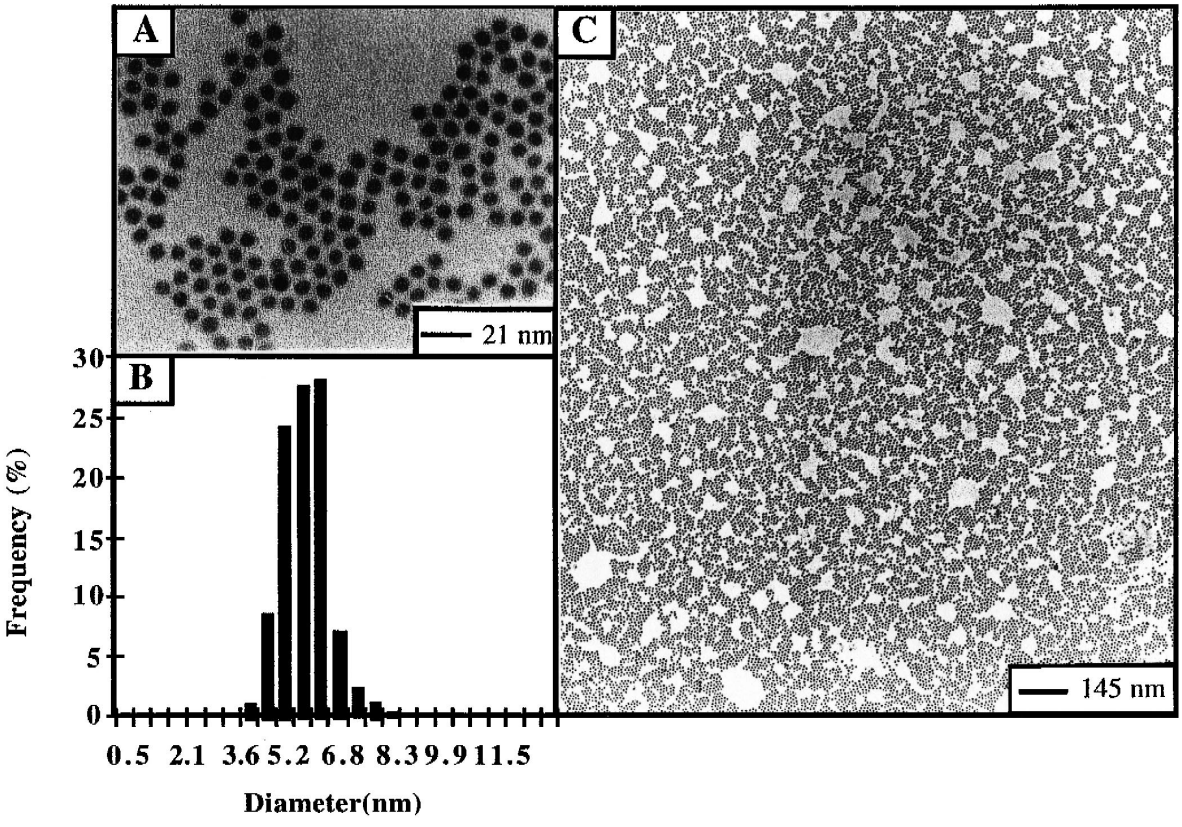

Fig. 2. TEM patterns at different magnification (A and B) and histogram of size of the hexagonal ordered monolayer of cobalt nanoparticles. This spontaneous self assembling is obtained by depositing a drop of solution on a TEM grid coated by amorphous carbon.

lauric acid and redispersed in hexane (particles **II**). For both cases, this chemical surface treatment highly improves the stability of cobalt exposed to air. Thus, cobalt nanoparticles could be stored without aggregation or oxidation for at least 1 week.

3.2. Characterization

The particles **I** are either dispersed in pyridine or can be obtained in powder form. After evaporation under nitrogen, the XRD pattern shows a large band centered at $q = 51.9°$ (i.e., $d = 2.03$ Å). However, the spectrum is poorly resolved so, the formation of cobalt boride ($q = 53.9°$; $d = 1.97$ Å) cannot be excluded. After annealing the powder under N_2 at 500°C for 2 h, the XRD spectrum shows the characteristic pattern of FCC cobalt metal [22]. This structure differs from the HCP structure of cobalt metal bulk phase. Note that the formation of FCC structure of cobalt metallic particles has been already reported in Ref. [23]. Reduction of cobalt ions by sodium borohydrure induces formation of various products. It has been well demonstrated in our previous paper [21] that the major part of the product is cobalt metal nanoparticles. However, it is rather difficult to discriminate the presence or absence of shell made of various cobalt derivatives.

To solve the problem, SAXS has been used. As a matter of fact, the electronic densities of the products vary with their composition. This permits to deduce formation of cobalt metal particles shelled by various derivatives and vice versa. The SAXS intensity, $I(q)$, of particles dispersed in pyridine as a function of the wave vector q is recorded. To differentiate between particles having a sharp interface or a shell structure, various adjustments of the Porod plot are compared to experimental data (Fig. 1).[1] Assuming that the particles are characterized by a sharp interface, the electronic density profile is square (insert, Fig. 1A). With a shell structure, the composition of

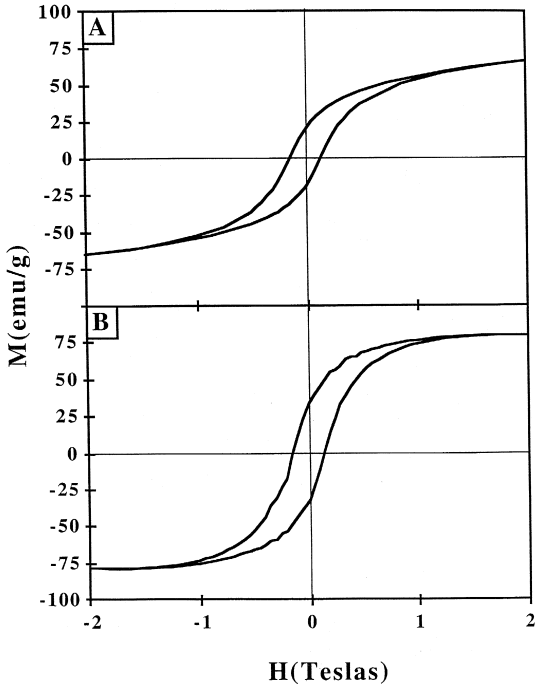

Fig. 3. Hysteresis magnetization loops obtained at $T = 3$ K. (A) Diluted (0.005% in volume) liquid solution of cobalt nanoparticles in hexane; (B) cobalt nanoparticles deposited onto freshly cleaved graphite (HOPG) and dried under argon to prevent oxidation.

[1] For a homogeneous sphere with a sharp interface, the scattering intensity is given by:

$$I(q) \approx P(q) = \phi_{pol} V F (\Delta\rho)^2 [B(qR)]^2$$

with

$$B(x) = \left[3\{\sin(x) - (x)\cos(x)\}/(x)^3\right]$$

where R, V, F, $\Delta\rho$, are the radius and volume of one particle, Thompson's factor (square of the classical electron radius, $F = 7.9 \times 10^{-26}$ cm^2) and the variation of the difference in the electron densities of the sphere and the surrounding medium, ρ_e and ρ_m, respectively. A convenient representation for homogenous diffusing spheres, is the Porod Plot, $I(q)q^4$ vs. q, which emphasizes the scattering at large q and then focuses on the interface as

$$\lim I(q)q^4 = 2\pi(\Delta\rho)^2 S \quad q \to \infty$$

where S is the total interfacial area.

On assuming spherical particles having a shell structure with an internal and external core, the scattering intensity is given by:

$$I(q) \approx P(q) = \phi_{pol} V F\{(\rho_m - \rho_e) B(qR_e) + (\rho_e - \rho_i) B(qR_i)\}$$

where ρ_e and ρ_i are the electron densities of the external and internal core of the particle, respectively. The particle radius is given by:

$$R = R_e + R_i$$

where R_i is the internal radius of the particles and R_e is the thickness of the shell.

The characteristic diameter of the particles D_c is related to the first maximum and minimum of this representation by D_c (nm) = $0.54/q_{max} = 0.9/q_{min}$.

the internal and external core has to be defined. In all cases, cobalt metal is taken as one component and a boron derivative is selected for the second component. To determine the compound, we take into account the products usually formed in homogeneous solution. Hence, the shell structure consists of cobalt metal and either B_2O_3 or Co_2B. We consider the following shell structures:

(i) the internal core is cobalt metal surrounded either by B_2O_3 or by Co_2B with an electronic density profile shown in the Fig. 1B and C inserts, respectively.
(ii) the internal core is made of Co_2B with an external shell of cobalt metal. The electronic profile is shown in the Fig. 1D insert.

The electronic densities of pure metallic cobalt, ρ_{Co}, pyridine, ρ_{pyr}, tri-octyl-phosphine, ρ_{top}, cobalt boride, ρ_{Co2B}, and borate, $\rho_{B_2O_3}$, are 2.43, 0.31, 0.29, 1.77 and 0.8 $e^-/Å^3$, respectively. Because the values of ρ_{pyr} and ρ_{top} are very close, it is impossible to discriminate between these two values and the electronic density of the surrounded medium of the spherical particles, ρ_m, is taken equal to ρ_{pyr}. A good correlation between the experimental data and the simulated curve is obtained for 8 nm spherical particles with 9% as size distribution (Fig. 1A). It is noticeable that the simulated and experimental data are in good agreement over a large q range especially for the positions of the maxima and minima and their relative intensities. The Porod plots corresponding to the various compositions that are obtained assuming a shell structure are shown in Fig. 1B, C and D. None of these different shell-core models, taking into account the possible products of the chemical reduction, could adjust the experimental data on the total q range value. From these data, it is concluded that homogeneous cobalt spheres with a sharp interface scatter. Taking into account the XRD pattern, it is reasonable to conclude that cobalt metallic particles are formed either without any shell made of derivatives or with an atomic layer, which cannot be detected in the present experimental conditions.

Deposition of a drop of solution on a carbon grid allows us to observe a large coverage of particles (Fig. 2C) locally arranged in a hexagonal network (Fig. 2A). The particle's average size deduced from the histogram (Fig. 2B) is 5.8 nm diameter with a polydispersity of 11%. This is in good agreement with the SAXS data.

Similar characterization is observed for particles **II** (which differs from **I** by their coating and the solvent used to dispersed the nanocrystals) behavior. There is no effect of the subsequent coating on the nature of the nanosized particles.

3.3. Magnetic properties

The magnetization curve at 150 K is simulated from the Langevin relationship

$$M(D) = M_s x\{\mathrm{ctnh}(\mu H/kT) - kT/\mu H\}$$

with $\mu = M_s \pi D^3/6$.

In a given field H, $M(D)$ is the magnetization of particles with diameter D.

The total saturation magnetization of the overall particles, M_s, is the sum of the saturation magnetization of each cobalt nanocrystal, $\mathcal{M}_S$:

$$M_s = N\mathcal{M}_S$$

where N is the number of particles. Assuming a log normal size distribution, the magnetization of particles at a given field, H, is:

$$M = \int M(D)\,P(D)\,\mathrm{d}D$$

where $P(D)$ is the number of particles of a given size, D. For the two set of samples, a good fit is obtained at 150 K. This indicates a super-paramagnetic behavior of the cobalt nanoparticles above the blocking temperature. Excellent agreement between the results obtained by TEM (5.8 nm), SAXS (8 nm) and magnetic measurements (5.5 nm) methods confirms the value for the particle average diameter and indicates non-directly on their stability. The difference between SAXS and the other techniques is due to the fact that with SAXS the TOP chains, coating the nanoparticles, are taken into account. The length of C8 chain is 1.2 nm, thus, the intrinsic cobalt size is found to be 5.6 nm. The saturation magnetization of nanocrystals dispersed in a solvent is not reached. It is estimated from the extrapolation of the plot of M/H vs. H. For particles **I** and **II**, it is 80 and 110 emu/g, respectively.

At 3 K, the ferromagnetic behaviors of isolated cobalt nanocrystals (dispersed in a solvent) and those arranged in 2D superlattices are compared in Fig. 3.

In the rising magnetic field, the magnetization of particles **I** dispersed in pyridine does not reach the saturation at least up to 2 T. The ratio M_r/M_s is

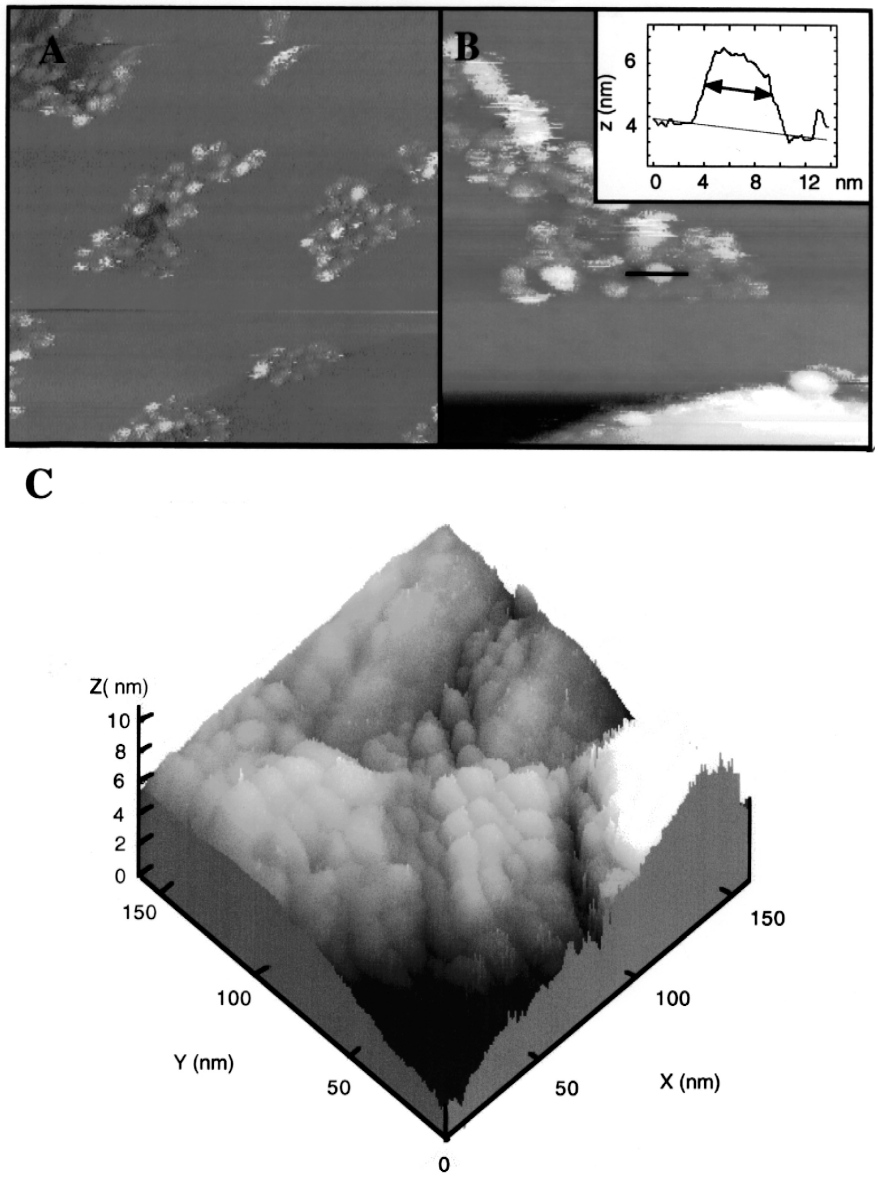

Fig. 4. Constant current mode STM images of cobalt particles deposited in diluted and concentrated solutions on dodecanthiol SAM ($I = 80$ pA, $V = 1$ V). The images are obtained at room temperature and in air. (A) Diluted solution. The image size is 166×166 nm^2. A hexagonal packing of nanoparticles is shown in the insert. (B) Diluted solution. The image size is 83×83 nm^2. The z-profile of the particles marked on the image is shown in the insert. (C) Concentrated solution. A 3D self-organisation ofnanoparticles is seen on this image. The image size is 150×150 nm^2.

0.25. M_r and M_s are the remanent and saturation magnetizations, respectively. The shape of hysteresis loop is very smooth. The blocking temperature is found to be equal to 58 K. The corresponding anisotropy constant is about 2.4×10^6 erg/cm^3. This is in a good agreement with the anisotropy constant reported for bulk FCC cobalt (2.7×10^6 erg/cm^3) [23].

When particles are organized in 2D superlattices, the saturation is reached at 1.5 T. The shape of

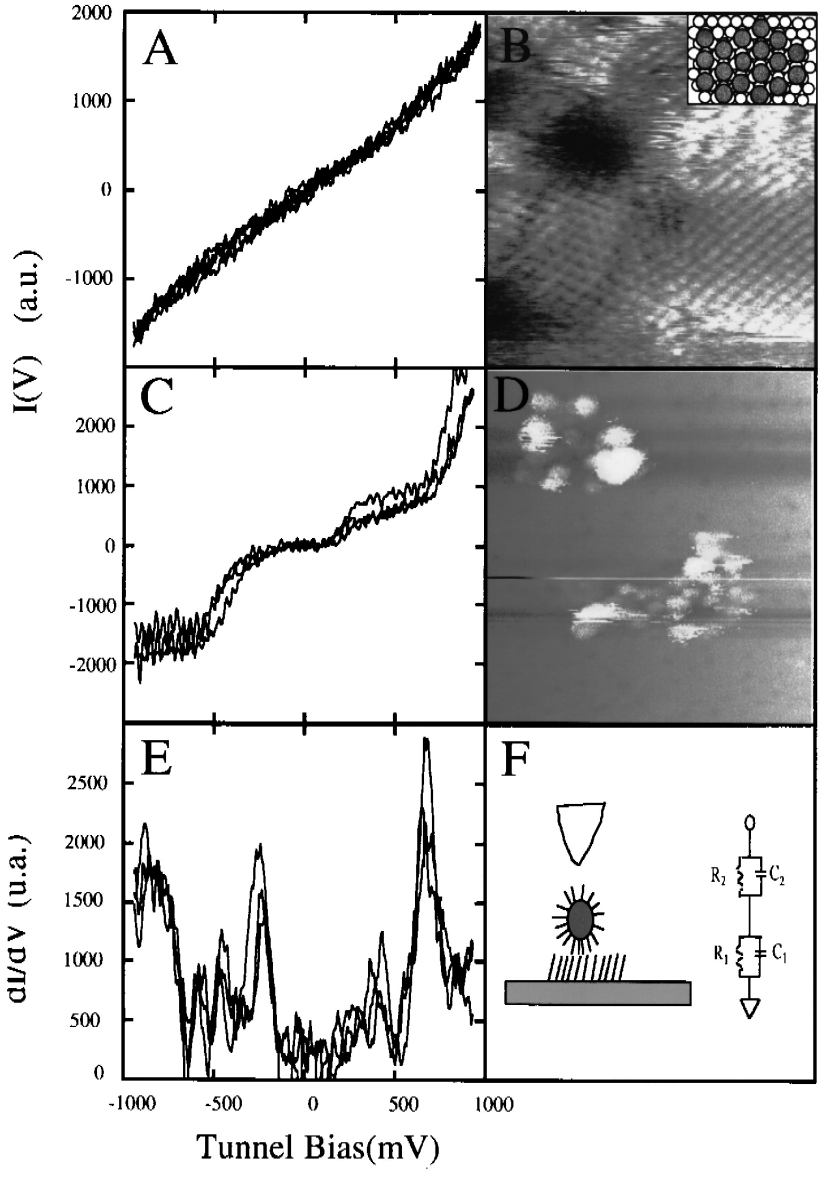

Fig. 5. Spectroscopic data and STM images of corresponding zones obtained at 77 K at different tip positions. (A) STS data: the tip is positioned on the SAM. (B) STM image of corresponding area of the SAM. insert is the sheme of the ($\sqrt{3} \times \sqrt{3}$)R30. Reconstruction of thiododecan on the Au(111) surfaces. (C) STS data: the tip is postionned above a small cluster of cobalt nanoparticles. (D) STM image of the cluster. (E) STS dI/dV vs. V plot for the cluster shown in D. (F) Equivalent tunneling junction scheme.

hysteresis loop differs from that observed with dispersed particles and tends to be square. The ratio M_r/M_s is 0.44. The blocking temperature is 63 K.

3.4. STM / STS experiments

Self-assembled well-organized monolayers (SAM) of dodecanthiol on the Au (111) surface are prepared as reported previously [24]. The structure of dodecanthiol monolayer on Au surface has been studied intensively [25–29]. The SAM patterns obtained by STM, in air, show characteristic feature of Au(111) surfaces covered by alkane thiols: small holes of 1–10 nm in size with an apparent depth corresponding to the thickness of one gold monolayer. This is probably a result of substrate vacancy islands generated by chemical erosion during the self-assembly process [29]. At higher resolution (Fig. 4B), the molecular ordering is clearly visible: the thiol molecules show a characteristic brush-like arrangement of the alkyl chains with the sulfur head group ordering into a $(\sqrt{3} \times \sqrt{3})R30°$ structures (insert, Fig. 4B). Fig. 5A shows the topographic image obtained at room temperature in air, once a drop of a dilute solution containing cobalt nanocrystals (0.01% in volume) is deposited onto the SAM. The coated particles are then ''grafted'' on the SAM by interdigitation between the dodecanethiol alkyl chains used to make the SAM and those to coat the nanocrystals. This stabilizes the nanoparticles on a conducting surface. Fig. 5A shows clusters made of few particles locally arranged on the surface. The constant current *z*-deflection scan performed across one particle is presented in the insert of Fig. 5B. While increasing the particle concentration dispersed in the solution by a factor 5 in some parts of the surface 3D self-assemblies of nanocrystals arranged in hexagonal close packing can be resolved (Fig. 5D). In the spectroscopic mode, the local I(V) characteristics of the tip–sample junction is analyzed for various positions over the SAM with or without of presence of nanocrystals. The data presented here have been recorded at 77 K, under a low pressure of helium exchange gas. A linear I(V) response is observed from the SAM covered gold surface without any particle (Fig. 4A). With a single particle (or a small cluster, Fig. 4D), a double tunneling junction (Fig. 4F), which exhibits highly non-linear I(V) spectrum if the tip is positioned directly above the particle(s) (Fig. 4C and E) is observed. This typical spectrum (see Fig. 4C) has the characteristics of the well-known Coulomb blockade effects. Fig. 4E shows a very large Coulomb blockade with a large asymmetric Coulomb gap (0.5 V).

4. Discussion

The extrapolated saturation magnetization of particles dispersed in pyridine is low (80 emu/g) compared to that of the FCC bulk material (162 emu/g). This large discrepancy can be attributed to the strong interactions between both pyridine and tri-octylphosphine with cobalt atoms at particles surfaces. Pyridine used as solvent is adsorbed at the particle interface. This electron donor kills the magnetization surface contribution [30]. This is confirmed by the fact that when similar particles are solubilized in hexane and coated by lauric acid, the saturation magnetization reaches 110 emu/g. This value is still lower than the bulk value but confirms changes in magnetization with the layer or solvent adsorbed at the nanocrystal surface.

Comparison of magnetic properties of particles **I** either dispersed in a solvent (considered as isolated) or arranged in 2D superlattices shows a change in the shape of hysteresis loop, in the ratio M_r/M_s value, in the blocking temperature and on the applied field needed to reach saturation magnetization.

When particles are arranged in 2D superlattices:

(i) the shape of the hysteresis loop is sharper compared to isolated particles;
(ii) the ratio M_r/M_s is 0.44 for self-assemblies and 0.25 for isolated particles;
(iii) the blocking temperature increases (63 K for self-assembled and 58 K for isolated nanocrystals); and
(iv) the saturation magnetization is reached (it is not with isolated particles).

These changes in magnetization properties can be attributed to an increase in the interaction between particles when they are deposited on a substrate. The origin of these interactions can be either dipolar or an exchange coupling. The latter can be excluded.

As a matter of fact, the distance between the edge of two neighboring particles is too large (2 nm), and there is no coalescence as it is clearly shown from TEM pattern (Fig. 2). Hence, the magnetic dipolar interactions between particles can be retained. These interactions could be either due to the self-organization with collective flip of magnetization between adjacent particles or to a high local volume fraction of particles randomly dispersed. To distinguish between these two possibilities, hysteresis loops have been recorded under various directions of the applied field toward the substrate. Preliminary data indicates that the shape of the hyteresis loop changes with the orientation of the applied field. This change can be attributed to magnetic dipole–dipole interactions induced by the self-organization of the particles on the substrate. These experiments have to be confirmed. From this, it seems reasonable to conclude that collective magnetic properties observed when particles are arranged in 2D superlattices are due to the self-organization in hexagonal network.

When coated cobalt nanoparticles are deposited onto the SAM, it acts as a brush: due to a weak interdigitation between the SAM and the chains of the particle coating, the nanoparticles are immobilized on the surface. Thus, the particles can be imaged without moving them irreversibly with the tip. The atomic steps of the gold substrate as well as the holes on the SAM act as nucleation centers to form the self-assembled state of cobalt nanoparticles. This defect on the surface corresponds to defect in the SAM and thus probably favors the penetration of the lauric acid chains inside the dodecanthiol SAM at the gold surfaces. It is important to note that the apparent height of the particle obtained by STM experiment is just about 2.5 nm, whereas its lateral apparent size is of 5.5 nm (insert, Fig. 4B) when TEM and SAXS data indicates spherical particles. This effect is probably due to the local density of charge (DOS) or tunneling barrier height perturbations, caused by the presence of the lauric acid chains at the surface of the particles, which may act as an insulating coat. Another possible explanation of this could be due to the shape of the tip. It seems to play a minor role, since the lateral apparent diameter of particles corresponds quite well to their physical size. The ohmic behavior observed on SAM without particles indicates that the SAM acts as a uniform insulating layer between the gold surface and the tip and does not modify significantly the DOS of the sample near the Fermi level. The Coulomb blockade effect, observed on nanoparticles deposited on SAM, is a consequence of the discreteness of electron charge: The transfer of an electron by tunneling between two initially neutral regions of capacitance C increases the electrostatic energy of the system by an amount $e^2/2C$. At small voltages $eV < e^2/2C$, the tunneling current is therefore suppressed due to this charging energy. Thus, a threshold voltage $V = e/2C$ is obtained in the tunneling current vs. bias voltage dependence. By plotting $\mathrm{d}I/\mathrm{d}V$ vs. the bias voltage V, further clear signatures are obtained (Fig. 5C), the Coulomb staircase. This effect results from the incremental increase of the current at bias voltages where it is energetically more favorable for each additional electron to cross the barrier. The observed asymmetry is probably due to partial net charge on the group of particles. We should mention here that we were able to obtain the STM images of the sample even after a sample exposure to air during 1 week. No significant changes of particle shape, their organization or spectroscopic data were found. It seems that the high stability of the particles under ambient conditions is due to their natural molecular coating.

5. Conclusion

In this paper, we describe the synthesis of metallic cobalt nanocrystals having 5.5 nm as average diameter and stable under air. This method allows an easy deposition of these objects as well as their fixation on the sample surface. This is usually obtained only by ''hard'' techniques. We are able to control the deposition of the particles, and their organization in 2D and 3D periodic structures. Magnetization studies show that collective behavior takes place in the self-assembled state. The changes in the hysteresis loop for a 2D network of cobalt nanoparticles are observed and attributed to collective flips of magnetization of groups of adjacent particles. Topographic STM images of coated cobalt particles clearly show the 2D and 3D local ordering of deposited particles as a function of their concentration. The substrate surface defects play the role of the nucle-

ation centers for 2D particle organizations. The low temperature STS (77 K) show the signature of the single electron tunneling across the ''Pt/Ir tip — single particle — gold substrate'' double tunneling junction.

Such a self-assembly state being an intermediate state between bulk and nanomaterials offers numerous possibilities not only for technological applications, but also for fundamental research.

References

[1] Nanoparticles superlattices, Annu. Rev. Phys. Chem. 49 (1998) 371.
[2] F. Burmeister, C. Schafle, T. Matthes, M. Bohmisch, J. Boneberg, P. Leiderer, Langmuir 13 (1997) 1983.
[3] C. Demaille, M. Brust, M. Tsionsky, A.J. Brad, Anal. Chem. 69 (1997) 2323.
[4] D.V. Averin, K.K. Likharev, in: B.L. Altshuler, P.A. Lee, R.A. Webb (Eds.), Mesoscopic Phenomena, North-Holland, New York, 1991, Chap. 6.
[5] G. Shön, U. Simon, Colloid Polym. Sci. 273 (1995) 202.
[6] E. Chi, M. Hartig, T. Dreschler, Th. Schwaak, C. Seidel, H. Fuchs, G. Schmid, Appl. Phys. A 66 (1998) S187.
[7] R.P. Andres, T. Bein, M. Dorogi, S. Feng, J.I. Henderson, C.P. Kubiak, W. Mahey, R.G. Osifchin, R. Reifenberger, Science 272 (1996) 1323.
[8] J.G.A. Dubois, J.W. Cerritsen, G. Schmid, H. van Kempen, Physica B 218 (1996) 262.
[9] S.E. Kutbakin, A.V. Danilov, A.L. Bogdanov, H. Olin, T. Claesan, Appl. Phys. Lett. 73 (1998) 24.
[10] M.P. Pileni, Langmuir 13 (1997) 3266.
[11] A.P. Alivisatos, Science 271 (1996) 933.
[12] A. Taleb, V. Russier, A. Courty, M.P. Pileni, Phys. Rev. B 59 (1999) 13350.
[13] L. Motte, F. Billoudet, M.P. Pileni, J. Phys. Chem. 99 (1995) 16425.
[14] L. Motte, F. Billoudet, E. Lacaze, J. Douin, M.P. Pileni, J. Phys. Chem. B 101 (1997) 138.
[15] A. Taleb, C. Petit, M.P. Pileni, Chem. Mater. 9 (1997) 950.
[16] A. Taleb, C. Petit, M.P. Pileni, J. Phys. Chem. B 102 (1998) 2214.
[17] S.A. Harfenist, Z.L. Wang, M.M. Alvarez, I. Vezmar, R.L. Whetten, J. Phys. Chem. 100 (1996) 13904.
[18] S.A. Harfenist, Z.L. Wang, R.L. Whetten, I. Vezmar, M.M. Alvarez, Adv. Mater. 9 (1997) 817.
[19] S.W. Chung, G. Markovich, J.R. Heath, J. Phys. Chem. B 102 (1998) 6685.
[20] C. Petit, A. Taleb, M.P. Pileni, Adv. Mater. 10 (1998) 259.
[21] C. Petit, A. Taleb, M.P. Pileni, J. Phys. Chem. B 103 (1999) 1805.
[22] JCPDS, International Centre for Diffraction Data File No. 15-806.
[23] J.M. Chen, C.M. Sorensen, K.J. Klabunde, G.C. Hadjipanayis, Phys. Rev. B 51 (1995) 11527.
[24] C. Petit, T. Cren, D. Roditchev, W. Sacks, J. Klein, M.P. Pileni, Adv. Mater. 11 (1999) 1198.
[25] L.C. Giancarlo, G.W. Flynn, Annu. Rev. Phys. Chem. 49 (1998) 297.
[26] C.A. Widrig, C.A. Alveo, M.D. Porteer, J. A.C.S. 113 (1991) 2805.
[27] Y.T. Kim, A.J. Bard, Langmuir 8 (1992) 1096.
[28] K. Edinger, A. Gölzhäuser, K. Demota, C. Wöll, M. Grunze, Langmuir 9 (1993) 4.
[29] J.P. Bucher, L. Santesson, K. Kern, Langmuir 10 (1994) 979.
[30] D.A. van Leeuwen, J.M. van Ruitenbek, L.J. de Jongh, A. Ceriotti, G. Pacchioni, O.D. Häberlen, N. Rösch, Phys. Rev. Lett. 73 (1994) 1432.